RESEARCH ARTICLE | APRIL 18 2024

Cation doping and oxygen vacancies in the orthorhombic $FeNbO_4$ material for solid oxide fuel cell applications: A density functional theory study

Xingyu Wang (王兴宇); David Santos-Carballal; Nora H. de Leeuw

J. Chem. Phys. 160, 154713 (2024)
https://doi.org/10.1063/5.0192749

The Journal of Chemical Physics ARTICLE pubs.aip.org/aip/jcp

Cation doping and oxygen vacancies in the orthorhombic $FeNbO_4$ material for solid oxide fuel cell applications: A density functional theory study

Cite as: J. Chem. Phys. 160, 154713 (2024); doi: 10.1063/5.0192749
Submitted: 20 December 2023 • Accepted: 22 March 2024 •
Published Online: 18 April 2024

Xingyu Wang (王兴宇),[1] David Santos-Carballal,[1,a)] and Nora H. de Leeuw[1,2,a)]

AFFILIATIONS

[1] School of Chemistry, University of Leeds, Leeds LS2 9JT, United Kingdom
[2] Department of Earth Sciences, Utrecht University, 3584 CB Utrecht, The Netherlands

[a)] **Authors to whom correspondence should be addressed:** d.santos-carballal@leeds.ac.uk and n.h.deleeuw@leeds.ac.uk

ABSTRACT

The orthorhombic phase of $FeNbO_4$, a promising anode material for solid oxide fuel cells (SOFCs), exhibits good catalytic activity toward hydrogen oxidation. However, the low electronic conductivity of the material specifically in the pure structure without defects or dopants limits its practical applications as an SOFC anode. In this study, we have employed density functional theory (DFT + U) calculations to explore the bulk and electronic properties of two types of doped structures, $Fe_{0.9375}A_{0.0625}NbO_4$ and $FeNb_{0.9375}B_{0.0625}O_4$ (A, B = Ti, V, Cr, Mn, Co, Ni) and the oxygen-deficient structures $Fe_{0.9375}A_{0.0625}NbO_{3.9375}$ and $FeNb_{0.9375}B_{0.0625}O_{3.9375}$, where the dopant is positioned in the first nearest neighbor site to the oxygen vacancy. Our DFT simulations have revealed that doping in the Fe sites is energetically favorable compared to doping in the Nb site, resulting in significant volume expansion. The doping process generally requires less energy when the O-vacancy is surrounded by one Fe and two Nb ions. The simulated projected density of states of the oxygen-deficient structures indicates that doping in the Fe site, particularly with Ti and V, considerably narrows the bandgap to ~0.5 eV, whereas doping with Co at the Nb sites generates acceptor levels close to 0 eV. Both doping schemes, therefore, enhance electron conduction during SOFC operation.

I. INTRODUCTION

$FeNbO_4$ gained initial recognition as a hydrogen sensor in the early 21st century.[1–9] In recent years, research on this material has diversified into various applications, including as dielectric ceramic materials,[10–13] anode materials for lithium-ion batteries, and catalytic electrodes.[14–23] Notably, an exploration of the orthorhombic phase with a disordered cation distribution as an alternative material for solid oxide fuel cell (SOFC) anodes has provided new insights into the stability and catalytic performance of such Fe-based anode materials.[17,19] Previous experimental studies have shown that the orthorhombic $FeNbO_4$ anode material exhibits robust resistance to sulfur poisoning and a good electric conductivity of ~0.7 S cm^{-1}, which is over ten times larger than the commonly used $La_{0.75}Sr_{0.25}Cr_{0.5}Mn_{0.5}O_3$[24–26] anode.

Despite these promising attributes, our previous work and other experimental results[27–33] have revealed that the bandgap of the pure orthorhombic $FeNbO_4$ material is around 2.2 eV, which limits its electronic conductivity. To address this limitation, Ti^{4+} dopants have been introduced to substitute both Fe^{3+} and Nb^{5+} ions.[19] However, the full impact of these dopants on the structural and electronic properties remains poorly understood. In this study, we have substitutionally doped the Fe and Nb sites of both the stoichiometric and O-deficient orthorhombic $FeNbO_4$ structures by the first-row transition metal atoms Ti, V, Cr, Mn, Co, and Ni. We have employed calculations based on the density functional theory (DFT) to evaluate the feasibility of incorporating these dopants into the material, fully characterizing their effect on the structural and electronic properties, which is crucial in guiding future experimental work.

II. COMPUTATIONAL METHODS

A. DFT calculations

We have employed the Vienna *Ab initio* Simulation Package, VASP (version 5.4.4),[34–37] to carry out the DFT calculations of the $FeNbO_4$ models. The frozen ion–electron interactions were modeled using the projector-augmented wave (PAW) method.[38] We have treated the following as valence electrons: Fe:$3p^6 3d^7 4s^1$, Nb:$4p^6 5s^1 4d^4 4s^2$, O:$2s^2 2p^6$, Ti:$3s^2 3p^6 3d^2 4s^2$, V:$3s^2 3p^6 3d^4 4s^1$, Cr:$3p^6 3d^5 4s^1$, Mn:$3p^6 3d^5 4s^2$, Co:$3p^6 3d^7 4s^2$, and Ni:$3p^6 3d^8 4s^2$. Despite partially breaking the Aufbau principle and differing from the ground state valence electronic configuration of the free atoms, VASP contains pseudopotential files using $3d^7 4s^1$ for Fe and $3d^4 4s^1$ for V, which resemble more closely the ground state valence electron distribution simulated in the bulk phases of these metals.[39,40] The valence electrons are allowed to relax during our simulations, and therefore, the references used for the valence electron distribution of these atoms are not really important, as they are identical across all our calculations. We have used the Perdew–Burke–Ernzerhof (PBE) generalized gradient approximation (GGA)[41] exchange–correlation functional for all the spin-polarized calculations. Partial occupancies were taken into account using the tetrahedron method with Blöchl corrections. The magnetic structure considered in this work is illustrated in Fig. 1, and the rationale for this choice is discussed in Sec. III A. To enhance the description of the electronic structures, we have incorporated the on-site Coulombic interaction (DFT + U)[42] for Fe-3d, Ti-3d, V-3d, Cr-3d, Mn-3d, Co-3d, and Ni-3d electrons with the U_{eff} values set at 4.3, 3.5, 3.5, 3.5, 4.0, 4.5, and 5.0 eV, respectively, based on previous studies.[26] After test calculations, the kinetic energy cutoff for the plane wave basis set was set at 500 eV, and the Henkelman algorithm was employed to calculate the Bader charges.[43] A 3 × 3 × 3 gamma-centered Monkhorst–Pack grid was used to simulate the bulk models, and structural optimizations were carried out using the conjugate gradient method, terminating when forces were converged within 0.01 eV/Å. The electronic energy was considered optimized when it exhibited a change of less than 10^{-5} eV between two consecutive self-consistent loops.

B. Doping energy

We represent the doping process in both stoichiometric ($Fe_{16}Nb_{16}O_{64}$) and O-deficient $Fe_{16}Nb_{16}O_{63}$ using the Kröger–Vink notation equations (1)–(4). This notation follows a set of conventions employed to describe the positions of point defects and charges within the crystal. We have designated A/B_xO_y as the metal oxide phases TiO_2, V_2O_5, Cr_2O_3, MnO_2, Co_3O_4, and NiO in their most stable structures, i.e., with the space groups P4_2/mnm, P2_1/m, R$\bar{3}$c, P4_2/mnm, Fd$\bar{3}$m, and Fm$\bar{3}$m, respectively. The lattice parameters for these structures are listed in Table S1. Note that the coefficient of O_2 is negative when the structure is doped with NiO at the Fe site and NiO, Cr_2O_3, MnO_2, and Co_3O_4 at the Nb site, indicating that this gas molecule is a reactant and not a product,

$$\frac{1}{x}A_xO_y(s) + Fe_{16}Nb_{16}O_{64}(s) \leftrightarrow Fe_{15}ANb_{16}O_{64}(s) + \frac{1}{2}Fe_2O_3(s) + \frac{2y-3x}{4x}O_2, \tag{1}$$

$$\frac{1}{x}B_xO_y(s) + Fe_{16}Nb_{16}O_{64}(s) \leftrightarrow Fe_{16}Nb_{15}BO_{64}(s) + \frac{1}{2}Nb_2O_5(s) + \frac{2y-5x}{4x}O_2, \tag{2}$$

$$\frac{1}{x}A_xO_y(s) + Fe_{16}Nb_{16}O_{63}(s) \leftrightarrow Fe_{15}ANb_{16}O_{63}(s) + \frac{1}{2}Fe_2O_3(s) + \frac{2y-3x}{4x}O_2, \tag{3}$$

$$\frac{1}{x}B_xO_y(s) + Fe_{16}Nb_{16}O_{63}(s) \leftrightarrow Fe_{16}Nb_{15}BO_{63}(s) + \frac{1}{2}Nb_2O_5(s) + \frac{2y-5x}{4x}O_2. \tag{4}$$

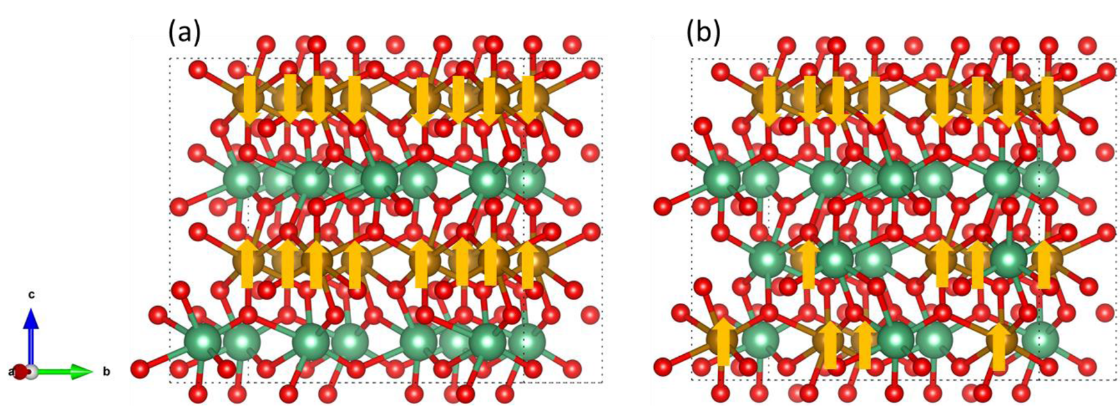

FIG. 1. (a) Stoichiometric and (b) O-deficient structures showing the magnetic configurations employed in this study. O is shown in red, Fe is shown in brown, and Nb is shown in green.

The doping energy (E_{doping}) is calculated as the sum of the energies of the products minus the sum of the energies of the reactants multiplied by their respective coefficients in the chemical equations (1)–(4).

III. RESULTS AND DISCUSSION

First, we have investigated the impact of the transition metal dopants on the structural and electronic properties of $FeNbO_4$. We have employed both the ordered stoichiometric structure and the O-deficient structure in the configuration with the largest probability, as identified in our previous work, see Fig. 1.[30] It is crucial to note that the lowest energy stoichiometric $FeNbO_4$ structure exhibits an ordered distribution of cations, characterized by a single ionic arrangement, whereas the O-deficient structure is disordered and is represented by multiple configurations.[30] In this work, we have used the 2 × 2 × 2 supercell of $FeNbO_4$, whose size is sufficient to capture the random cation distribution and simulate the bulk properties of the doped $Fe_{0.9375}A_{0.0625}NbO_4/FeNb_{0.9375}B_{0.0625}O_4$ and oxygen-deficient $Fe_{0.9375}A_{0.0625}NbO_{3.9375}/FeNb_{0.9375}B_{0.0625}O_{3.9375}$ configurations. Specifically, when introducing one dopant atom into the Fe or Nb sites of the 2 × 2 × 2 supercell, the stoichiometry was reduced from 1 to 0.9375, where the subscript 3.9375 means that one oxygen vacancy was generated in the simulation cell. After testing various magnetic structures, we determined that the stoichiometric material adopts an antiferromagnetic configuration, where the alternating Fe layers along the c axis have opposite spin directions, see Figs. 1(a) and S1. In contrast, the most stable configuration for the O-deficient structure involves spins of the Fe in the layer containing only these cations aligning in the opposite direction to the spins in the mixed layers, which are parallel, as shown in Fig. 1(b).

A. Effect of dopants on $FeNbO_4$

1. Structural properties

The stoichiometric $FeNbO_4$, modeled as a 2 × 2 × 2 supercell and belonging to the space group Pbcn, comprises 16 Fe, 16 Nb, and 64 O atoms ($Fe_{16}Nb_{16}O_{64}$). Given that all Fe and Nb ions reside in the same Wyckoff 4c site, our approach involves selectively substituting one Fe and one Nb site at a time for the doping process, see Fig. 2. Initially, we have scrutinized the effect of dopants in the Fe site on the lattice parameters, which are summarized in Table I. Across all structures with dopants in the Fe site, we observed a tendency for lattice elongation along the a axis, while the Co and Ni dopants resulted in a reduction in the b and c lengths of the cell. Our computations indicate that post-doping, the α and γ angles of all structures have remained at 90°, while the β angle deviated by no more than 0.08° from the ideal right angle of the parent material. The y coordinate experienced a slight overestimation in comparison with the ideal 4c Wyckoff position value of 0.1786. In addition, we have computed the volume as $V = a \times b \times c$

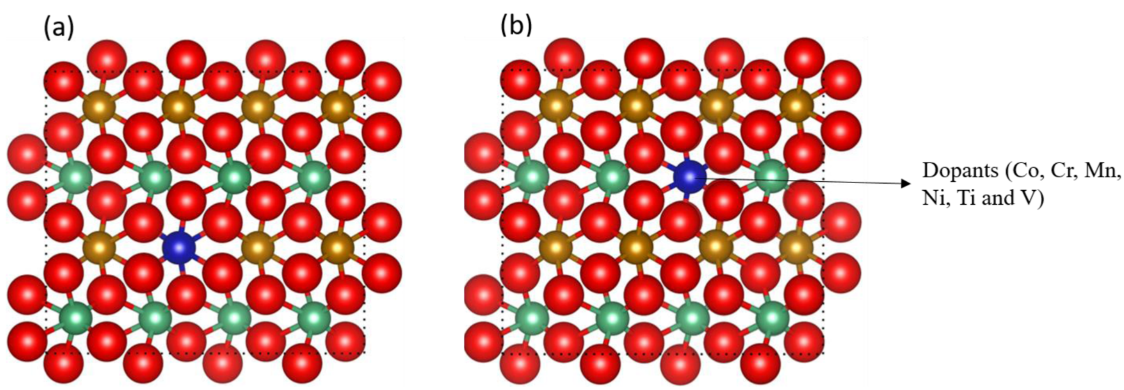

FIG. 2. Optimized structures of $FeNbO_4$ with Co, Cr, Mn, Ni, Ti, and V dopants on the (a) Fe site and (b) Nb site. O is red, Fe is brown, Nb is green, and dopants are dark blue.

TABLE I. Lattice parameters (a, b, and c), lattice angles (α, β, and γ), y coordinate of dopants, and volume of the $FeNbO_4$ structure with dopants incorporated at the Fe site.

A, B	a (Å)	b (Å)	c (Å)	α (°)	β (°)	γ (°)	y	V (Å^3)	$\Delta V/V$ (%)
Stoichiometric	9.407	11.380	10.046	90	90	90	0.1786	1075.627	⋯
Ti	9.421	11.388	10.062	90	90.01	90	0.1809	1079.584	0.368
V	9.414	11.387	10.056	90	89.94	90	0.1828	1077.887	0.210
Cr	9.411	11.382	10.048	90	89.97	90	0.1858	1076.271	0.060
Mn	9.417	11.394	10.039	90	90.15	90	0.1823	1077.232	0.149
Co	9.412	11.376	10.045	90	89.97	90	0.1806	1075.459	−0.015
Ni	9.408	11.375	10.045	90	89.92	90	0.1833	1075.045	−0.054

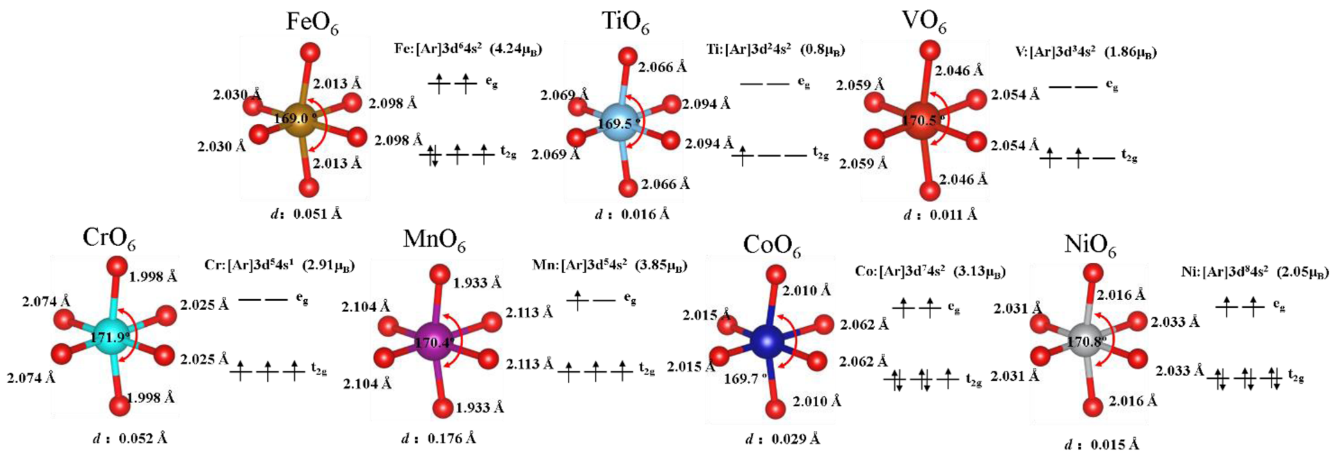

FIG. 3. Octahedral geometry and orbital splitting of dopants in the Fe site of the stoichiometric structure. The Jahn–Teller distortion is defined as $d_{JT} = (d_{e1} + d_{e2})/2 - d_a$, where d_{e1}, d_{e2}, and d_a indicate the equatorial bond distances 1 and 2 and the axial bond distance, respectively.

$\times \sqrt{1 - \cos^2\alpha - \cos^2\beta - \cos^2\gamma + 2\cos\alpha\cos\beta\cos\gamma}$ and the volume change as $\frac{\Delta V}{V} = \frac{V_{doped} - V_{undoped}}{V_{undoped}}$. Our findings indicate that structures doped with Co or Ni underwent a marginal compression along the *b* and *c* directions. In contrast, doping with Ti, V, Cr, and Mn led to a volume expansion with the Ti-doped structure exhibiting the most significant increase at 0.368%. Notably, the observed effects of first row transition metal dopants on volume align closely with previous research, where the introduction of Ti and Cr on the Mn site of $NaMnO_2$ resulted in volume stretching, while Co and Ni, possessing larger atomic numbers than Mn, led to volume compression.[44]

For a transition metal atom with an octahedral geometry, the five d orbitals are split into three degenerate lower-energy t_{2g} orbitals and two degenerate higher-energy e_g orbitals. However, those orbitals are unstable and break the degeneracy, resulting in the elongation or shortening of one of the three C_4 rotation axes, which is known as the Jahn–Teller distortion. We found that the octahedral geometries of all dopants, also including Fe and Nb in the stoichiometric structure, show Jahn–Teller distortion, where each of the three pairs of identical bonds have different lengths to the other two and the axial angle deviates from 180°, see Figs. 3 and 4. We have calculated the Jahn–Teller distortion as $d_{JT} = (d_{e1} + d_{e2})/2 - d_a$, where d_{e1}, d_{e2}, and d_a indicate the equatorial bond distances 1 and 2 and the axial bond distance, respectively. Our simulations show that the uneven occupation of electrons in e_g orbitals leads to a stronger Jahn–Teller distortion than the partial occupation of the t_{2g} orbitals, as found in previous studies.[45,46] For example, the single electron in the e_g orbital of Mn leads to the largest distortion of 0.176 Å found in this work when doping into the Fe sites of the stoichiometric structure. In addition, we found weak Jahn–Teller distortions of Fe, Ti, V, and Co octahedra below 0.051 Å because of the uneven occupation of electrons in the t_{2g} levels. For the Cr and Ni dopants,

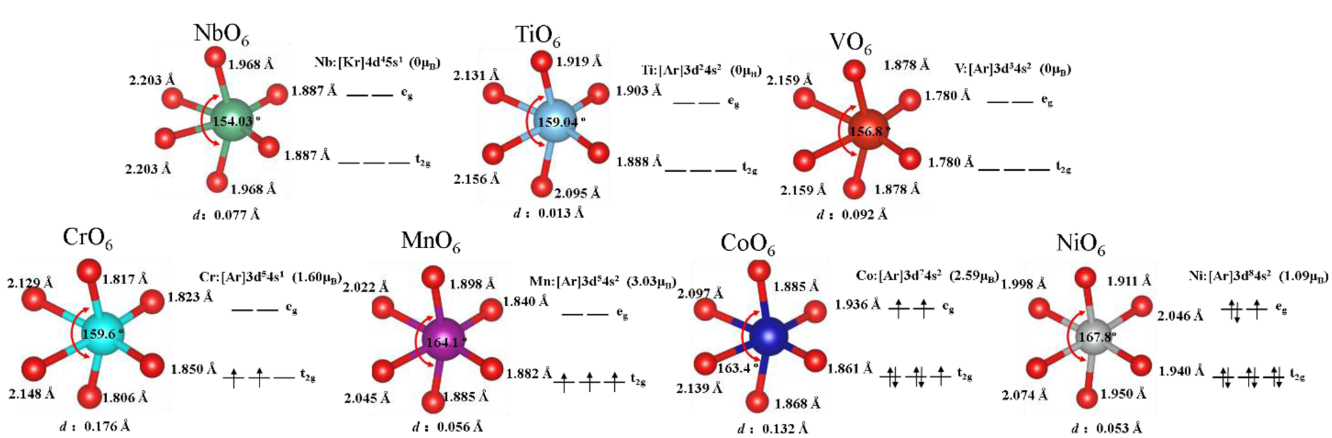

FIG. 4. Octahedral geometry and orbital splitting of dopants in the Nb site of the stoichiometric structure. The Jahn–Teller distortion is defined as $d_{JT} = (d_{e1} + d_{e2})/2 - d_a$, where d_{e1}, d_{e2}, and d_a indicate the equatorial bond distances 1 and 2 and the axial bond distance, respectively.

the electrons are distributed evenly in the t_{2g} or e_g levels, and thus, we would not expect distortion. However, we found weak distortions of 0.052 and 0.015 Å for Cr and Ni, respectively, that are even larger than for other ions with uneven occupation of the t_{2g} orbitals. The Jahn–Teller distortion found here follows the order $d_{JT}(\text{Mn}) > d_{JT}(\text{Fe}) > d_{JT}(\text{Cr}) > d_{JT}(\text{Co}) > d_{JT}(\text{Ti}) > d_{JT}(\text{Ni}) > d_{JT}(\text{V})$.

Our calculations indicate that the t_{2g} and e_g levels of Nb are empty in the stoichiometric structure. We also found that after doping the Nb site with Ti and V, the t_{2g} and e_g remain unoccupied, whereas only three electrons occupy the t_{2g} level of the Mn dopant, which explains the weak Jahn–Teller distortions of up to d_{JT} = 0.092 Å for the V ion, see Fig. 4. Despite an odd number of electrons distributed in the e_g level of Ni, we only found a small Jahn–Teller effect with a distortion of 0.053 Å. Cr and Co with a high spin electron distribution should exhibit weak Jahn–Teller distortions owing to the uneven occupation of their t_{2g} orbitals. However, we found large distortions of 0.176 and 0.132 Å for Cr and Co, respectively. Note that the distortion of the axial angle is larger for the dopants in the Nb site than in the Fe site. We speculate that the lack of correlation between the expected weak and strong Jahn–Teller distortions can be explained not only by the elongation or shortening of the axial bond, but also by the bending of the axial axis. We do not discuss the Jahn–Teller effect in the O-deficient structures because the introduction of oxygen vacancies leads to dangling bonds.

Table II shows that structures containing dopants at the Nb sites are compressed in all three crystallographic directions, barring the expanded *c* parameter observed in the Ti-doped structure. Our simulations show that the lattice structure tends to adopt a triclinic form, with all lattice angles deviating from 90° by no more than 0.18°. Furthermore, the y coordinates of dopants at the Nb sites tend to be underestimated compared to the value in the parent material of 0.1786, except for the structure containing V. Our calculated volumes for the doped structures are consistently smaller than those of pure $FeNbO_4$, with the Mn-doped material, exhibiting the most significant reduction of 0.556%. In general, our findings indicate that doping the Nb site induces a greater degree of symmetry breaking compared to doping the Fe site, resulting in the formation of triclinic structures. Crucially, our calculations reveal a volume decrease solely for $FeNb_{0.9375}B_{0.0625}O_4$, with respect to $FeNbO_4$, underscoring the prominent role of Nb site doping in reducing the overall volume of the material.

TABLE III. Atomic Bader charges (*q*) in the doped $FeNbO_4$ structure.

	Fe site				Nb site			
A, *B*	q_A (e)	q_O (e)	q_{Fe} (e)	q_{Nb} (e)	q_B (e)	q_O (e)	q_{Fe} (e)	q_{Nb} (e)
Stoichiometric	⋯	−1.14	+1.86	+2.72	⋯	−1.14	+1.86	+2.72
Ti	+2.11	−1.15	+1.86	+2.72	+2.44	−1.14	+1.86	+2.72
V	+1.97	−1.15	+1.86	+2.72	+2.31	−1.14	+1.86	+2.72
Cr	+1.84	−1.14	+1.86	+2.72	+2.06	−1.13	+1.86	+2.72
Mn	+1.81	−1.14	+1.86	+2.72	+1.92	−1.13	+1.86	+2.72
Co	+1.67	−1.14	+1.86	+2.72	+1.63	−1.13	+1.86	+2.72
Ni	+1.52	−1.14	+1.86	+2.72	+1.41	−1.12	+1.86	+2.72

The Bader charges for both $Fe_{0.9375}A_{0.0625}NbO_4$ and $FeNb_{0.9375}B_{0.0625}O_4$ structures are presented in Table III. We observe a consistent decrease in the Bader charges of first row transition metal dopants at the Fe site, following the order $q_{Ti} > q_V > q_{Cr} \approx q_{Mn} > q_{Co} > q_{Ni}$, which is consistent with their respective positions in the Periodic Table. Our calculations indicate that the Bader charges of O, Fe, and Nb remain constant with respect to the stoichiometric structure, except for Ti- and V-doped structures, where the Bader charge of oxygen exhibits a marginal increase. We noted a similar trend in the Bader charges of dopants between $FeNb_{0.9375}B_{0.0625}O_4$ and $Fe_{0.9375}A_{0.0625}NbO_4$. Our DFT calculations indicate that Bader charges of dopants tend to be larger at the Nb site than at the Fe site. This observation suggests a greater likelihood for the Nb site to form stronger ionic interactions with the crystal than its Fe counterpart.

Next, we have calculated the magnetic moments of the cations in the stoichiometric and doped materials, as shown in Table IV. The magnetic moment of Fe is underestimated at 4.27 μ_B, a value in close agreement with previous findings.[33] The magnetic moments of the dopants tend to increase with atomic number from Ti to Mn, followed by a decrease from Mn to Ni. Moreover, the valence states of cations in the stoichiometric and doped materials can be deduced from their magnetic moments. In the $Fe_{0.9375}A_{0.0625}NbO_4$ structure, we have approximated the magnetic moments of dopants to the nearest integer, resulting in $m_s(\text{Fe}) = 5\ \mu_B$, $m_s(\text{Nb}) = 0\ \mu_B$, $m_s(\text{Ti}) = 1\ \mu_B$, $m_s(\text{V}) = 2\ \mu_B$, $m_s(\text{Cr}) = 3\ \mu_B$, $m_s(\text{Mn}) = 4\ \mu_B$,

TABLE II. Lattice parameters (*a*, *b*, and *c*), lattice angles (*α*, *β*, and *γ*), y coordinate of dopants, and volume of the $FeNbO_4$ structure with dopants incorporated at the Nb site.

A, *B*	*a* (Å)	*b* (Å)	*c* (Å)	*α* (°)	*β* (°)	*γ* (°)	*y*	*V* (Å^3)	*ΔV*/*V* (%)
Stoichiometric	9.407	11.380	10.046	90	90	90	0.1786	1075.627	⋯
Ti	9.402	11.374	10.052	89.97	89.82	90.06	0.1764	1075.036	−0.055
V	9.390	11.378	10.031	90	89.92	90	0.1817	1071.851	−0.351
Cr	9.387	11.380	10.026	89.97	89.90	90.05	0.1750	1071.000	−0.430
Mn	9.383	11.355	10.039	90.04	89.82	90.02	0.1630	1069.650	−0.556
Co	9.391	11.369	10.034	89.91	89.95	89.93	0.1684	1071.420	−0.391
Ni	9.385	11.368	10.038	89.85	89.83	90.16	0.1525	1071.011	−0.429

TABLE IV. Atomic magnetic moments (m_s) and valence states (VS) of the doped $FeNbO_4$ structure.

	Fe site		Nb site	
A, *B*	m_s (μ_B)	VS	m_s (μ_B)	VS
Stoichiometric	4.27-(Fe)	+3	0-(Nb)	+5
Ti	0.80	+3	0	+4
V	1.86	+3	0	+5
Cr	2.91	+3	1.60	+4
Mn	3.85	+3	3.03	+4
Co	3.13	+2	2.59	+2
Ni	2.05	+2	1.09	+1

m_s(Co) = 3 μ_B, and m_s(Ni) = 2 μ_B. All cations, including dopants, are in octahedral coordination, splitting the 3d orbital into three degenerate t_{2g} orbitals (d_{xy}, d_{xz}, and d_{yz}) and two also degenerate e_g orbitals ($d_{x^2-y^2}$ and d_{z^2}). Specific magnetic arrangements for Fe-substituted structures reveal that Cr, Mn, Ti, and V are in the +3 valence state, while Co and Ni are in the +2 oxidation state. In addition, we have calculated the magnetic moment of dopants at the Nb site, all displaying a relatively low-spin state. Our calculations show that only the valence state of Ni was underestimated at +1, which is a state uncommon for Ni. Comparing valence states in both the Fe and Nb sites, we observe that, except for the Co dopant, the magnetic moments of the other dopants are lower than the corresponding values at the Fe site. This correlates with an increase in valence states from +2 to +4 for Cr, Mn, and Ti and from +3 to +5 for V. Furthermore, the valence states of Co and Ni in the $Fe_{0.9375}A_{0.0625}NbO_4$ structure is smaller than that of the substituted Fe^{3+}, suggesting that oxygen donated electrons to these two dopants, a trend that is also evident in Ti-, Cr-, Mn-, Co-, and Ni-doped $FeNb_{0.9375}B_{0.0625}O_4$ structures.

Shannon's effective radius for each dopant and their doping energies into $FeNbO_4$ are detailed in Table V. Shannon's reported effective ionic radii[26] are contingent on the valence and spin states of the transition metal atom. When Co and Mn occupy the Fe site, two possible magnetic structures emerge: high-spin states with magnetic moments of 3 and 4 μ_B, respectively, or low-spin states, with magnetic moments of 1 and 2 μ_B, respectively, see Fig. 4. Our calculations indicate that the magnetic moments of Co and Mn align closely with high-spin states, measuring 3 and 4 μ_B, respectively. In contrast, Ti, V, Cr, and Ni exhibit only one magnetic configuration, as illustrated in Fig. 4. Our calculations show that only Ti^{3+} possesses a larger radius (0.670 Å) than Fe^{3+} in the parent structure, whereas Mn^{3+} and Fe^{3+} have very similar sizes, which is expected from their relative positions in the Periodic Table, see Table V. Furthermore, the radii of V^{3+} and Cr^{3+} atoms, calculated as 0.640 and 0.615 Å, respectively, are smaller than Fe^{3+}. In contrast, Co^{2+} and Ni^{2+} feature larger radii than Fe^{3+}, attributed to their distinct oxidation states. The calculated doping energies imply that inserting V^{3+}, Cr^{3+}, or Mn^{3+} is generally more facile than replacing Fe with Co^{2+}, Ni^{2+}, or Ti^{3+}. In addition, we found that dopant size correlates with doping energy, evidenced by the sequence $R_{Co} > R_{Ni} > R_{Ti} > R_{Mn} > R_V > R_{Cr}$ and the order of doping energy as $E_{Ti} > E_{Co} > E_{Ni} > E_V > E_{Mn} > E_{Cr}$. This suggests that dopants with smaller radii find it easier to replace Fe than those with large radii with the exception of Ti and V.

Table V shows that only Ti^{4+}, V^{5+}, Cr^{4+}, and Mn^{6+} have smaller radii than Nb^{5+}. Note that the effective radius of Ni in the 1+ oxidation state is not reported in Shannon's table. Our calculated doping energies indicate that incorporating V at the Nb site is the easiest process, while the inclusion of other cations, particularly Cr or Co, is less favorable. However, no discernible relationship is apparent between the radii of first-row transition metal atoms and their doping energies, indicating a substantial disparity with the size of Nb, a second-row transition metal atom. In general, the radii of dopants on the smaller Fe site are larger than on the larger Nb site, except for Co and Ni, which explains the larger doping energies on the latter site.

TABLE V. Shannon effective ionic radii (*R*) for dopants and doping energy (E_d) for the doped $FeNbO_4$ structure.

	Fe site		Nb site	
A, *B*	*R* (Å)	E_d (eV)	*R* (Å)	E_d (eV)
Stoichiometric	0.645	⋯	0.690	⋯
Ti	0.670	1.67	0.605	2.30
V	0.640	0.85	0.540	1.34
Cr	0.615	0.12	0.550	7.22
Mn	0.645	0.26	0.530	3.60
Co	0.745	1.26	0.745	9.17
Ni	0.690	0.92	⋯	3.70

2. Projected density of states (PDOS)

We have plotted the projected density of states (PDOS) for both stoichiometric and doped $FeNbO_4$ to elucidate the impact of the first-row transition metal dopants on the electronic structures.

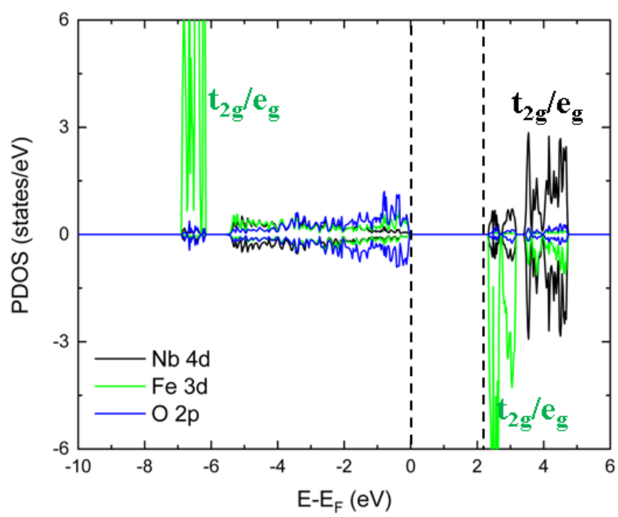

FIG. 5. Projected density of states (PDOS) for the stoichiometric $FeNbO_4$.

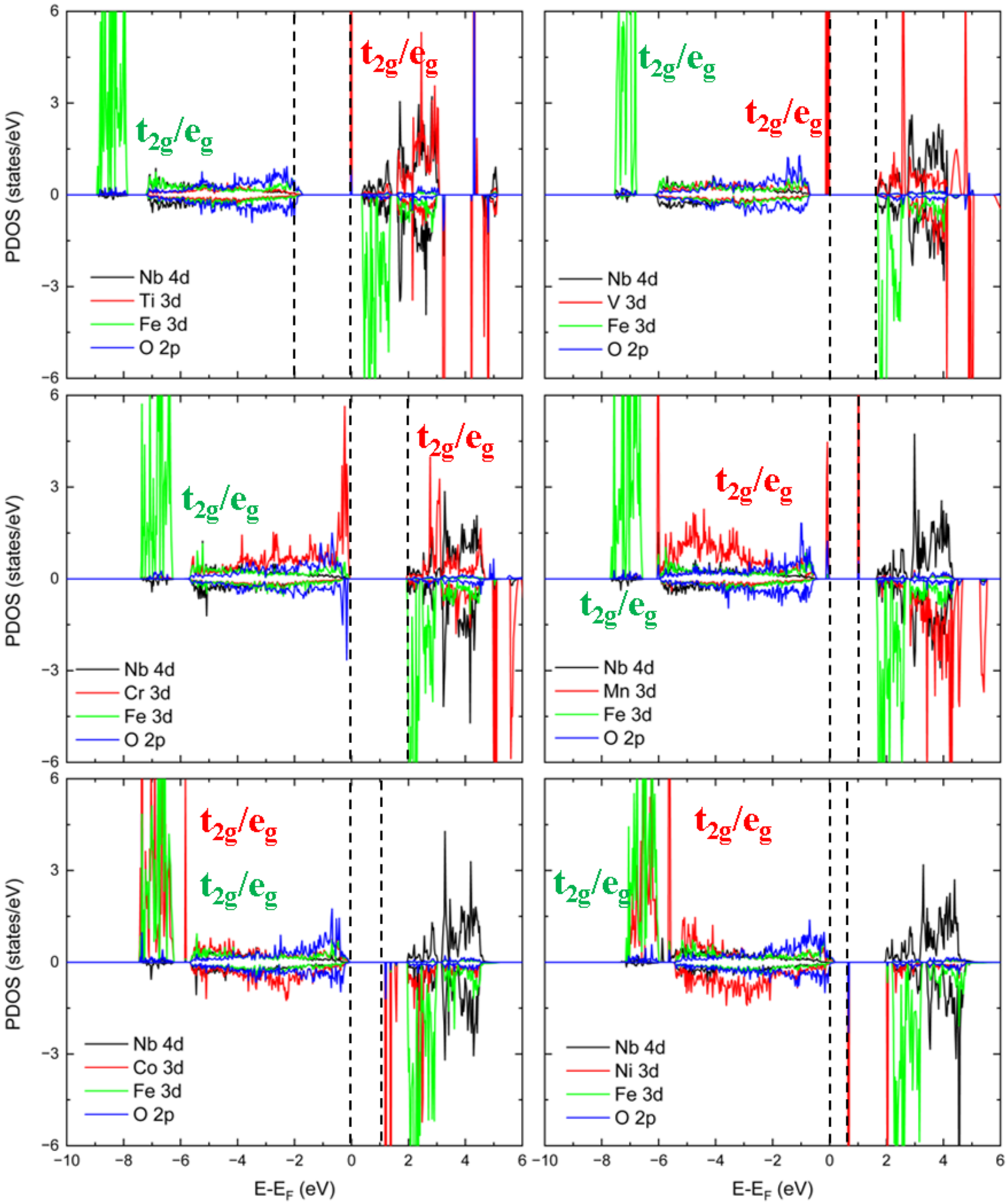

FIG. 6. Projected density of states (PDOS) of $FeNbO_4$ doped with (a) Ti, (b) V, (c) Cr, (d) Mn, (e) Co, and (f) Ni on the Fe site.

The electronic states of the first nearest neighbor (NN) ions to the dopant site were selected for display, owing to the symmetry of the stoichiometric structure, see Fig. S3. Figure 5 illustrates that stoichiometric $FeNbO_4$ behaves as a semiconductor with a PDOS bandgap of 2.2 eV. The t_{2g} and e_g valence levels of Fe^{3+}, which are fully occupied, appear at −7 eV with a separation of ~1.2 eV in the majority spin channel. The empty t_{2g} and e_g states of Fe^{3+} are located at around 2 eV in the opposite minority spin channel, leading to a separation of 9 eV between them, which is also observed in the previous work on Fe_3O_4.[47] Meanwhile, the t_{2g} and e_g orbitals of Nb are exclusively observed in the conduction band above 3 eV, given that this cation is fully oxidized, having transferred all its 4d electrons to the oxygen anions. The 2p state of oxygen is delocalized in the valence region, from −5.5 to 0 eV.

The electronic structure of $FeNbO_4$ doped at the Fe site with first-row transition metal atoms is depicted in Fig. 6. It is noteworthy that in the Ti-, V-, and Cr-doped structures, the t_{2g} valence orbitals of the dopants progressively shift into the delocalized valence band region. In the Ti- and V-doped structures, we observe only one localized t_{2g} orbital below the Fermi level, while in the Cr- to Ni-doped structures, most 3d states are distributed in the valence region from −6 to 0 eV. The PDOS of the Co- and Ni-doped structures indicate that the t_{2g} and e_g orbitals are situated near −7 eV, with the empty e_g orbitals appearing in the conduction band. Our simulations suggest that with an increase in the atomic number of the dopant, the t_{2g} and e_g orbitals gradually become fully occupied from Cr to Ni, corresponding to the electronic occupations of $Ti^{e_g}_{t_{2g}\uparrow}$, $V^{e_g}_{t_{2g}\uparrow\uparrow}$, $Ce^{e_g}_{t_{2g}\uparrow\uparrow\uparrow}$, $Mn^{e_g\uparrow}_{t_{2g}\uparrow\uparrow\uparrow}$, $Co^{e_g\uparrow\uparrow}_{t_{2g}\uparrow\downarrow\uparrow\downarrow\uparrow}$, and $Ni^{e_g\uparrow\uparrow}_{t_{2g}\uparrow\downarrow\uparrow\downarrow\uparrow\downarrow}$. In addition, we found that after doping with Mn, Co, or Ni, acceptor levels comprising t_{2g} and e_g orbitals are generated between the valence band maximum (VBM) and the conduction band minimum (CBM) of the parent material. Generally, doping proves beneficial in reducing the bandgap, especially for the structure containing Ti on the Fe site, where the Fermi level is close to the CBM, in agreement with experimental findings.[28] The impact of dopants on the PDOS of Fe, Nb, and O is negligible with respect to the parent material.

Our calculations show that when Ti and V are doped into the Nb site of the stoichiometric structure, there are no bands in the valence region, as these cations lack electrons. In the Cr- and Mn-doped structures, the t_{2g} and e_g orbitals appear in the valence band region, but due to the incomplete occupation of 3d orbitals, we still observe states in the conduction band region. With increasing atomic numbers, the electrons in the 3d orbitals of Co- and Ni-doped structures tend to occupy states further toward −7 eV. In all the structures, the 3d orbitals of Fe, 4d orbitals of Nb, and 2p orbitals of O show a similar distribution to the parent structure, indicating that the effect of doping is minimal and can be disregarded (Fig. 7).

Despite finding that the d-band centers of the dopants appear at particular positions in the DOS, as well as changes in the cell volume and electronic bandgap of the structures owing to the incorporation of transition metal atoms, no trend or relationship between them could be identified, see Tables S2–S4.

B. Effect of dopants on the O-deficient $FeNbO_4$

Next, we introduced one oxygen vacancy into the supercells and subsequently again incorporated first-row transition metal dopants into the Fe and Nb sites to investigate their effect on the geometric and electronic properties. Figure 8 illustrates four distinct configurations of the O-deficient $FeNbO_4$ structure, i.e., when the oxygen vacancy is surrounded by (*i*) three Fe (FFF), (*ii*) two Fe and one Nb (FFN), (*iii*) one Fe and two Nb (FNN), and (*vi*) three Nb (NNN) cations. However, we observed that the NNN type oxygen vacancy migrated and transformed into the FNN type following optimization.

The lattice parameters of the O-deficient structures are presented in Table VI. Our calculations reveal that the introduction of oxygen vacancies induces an expansion in the lattice parameters *a*, *b*, and *c*. The most significant expansions in *a* and *c* are observed in the FNN-vacancy type structure, while the largest expansion in *b* is found in the FFN-vacancy type structure. Moreover, a slight distortion in the crystal shape is noted, with all angles deviating from 90°, see Table VI. The enlarged lattice parameters and distorted cell shape collectively contribute to a volume expansion in the structure. This expansion can be rationalized by considering the larger size of Fe^{2+} compared to Fe^{3+} cations when the latter undergo reduction upon the formation of an O vacancy, as reported in previous studies.[48,49] The formation energy of the oxygen vacancy was calculated as $E_{vac} = E_{Fe_{16}Nb_{16}O_{63}} - E_{Fe_{16}Nb_{16}O_{64}} + \frac{1}{2}E_{O_2}$, where $E_{Fe_{16}Nb_{16}O_{63}}$ and $E_{Fe_{16}Nb_{16}O_{64}}$ represent the total energies of the O-deficient $FeNbO_4$ and stoichiometric $FeNbO_4$, respectively, and E_{O_2} refers to the total energy of the oxygen molecule in the triplet ground state. The calculated vacancy formation energies indicate that the process is endothermic for the three types of vacancies considered in this study, ranging between 2.14 eV for FFF and 4.13 eV for FNN. This suggests that the material will not spontaneously undergo reduction. The FNN-type vacancy exhibits the largest volume expansion, consistent with its higher number of surrounding Nb atoms. The decreasing order of formation energy for the oxygen vacancies is $E^{FNN}_{vac} > E^{FFN}_{vac} > E^{FFF}_{vac}$. Using the entropy of an O_2 molecule from thermodynamic tables,[50] we have calculated its contribution to the energies at various temperatures. We found that the entropy contribution of half an O_2 molecule is $-T\Delta S$ = 2.14 eV at 1580 K, which compensates exactly the energy of −2.14 eV for the process represented in Eq. (5). Thus, we expect this material to reduce spontaneously between 1580 and 1800 K, which is the melting point. Note that we have assumed that the entropy of the bulk solid phases does not change in this analysis.

$$Fe_{16}Nb_{16}O_{64}(s) \leftrightarrow Fe_{16}Nb_{16}O_{63}(s) + \frac{1}{2}O_2(g). \quad (5)$$

1. Structural properties

First, we considered the substitutional doping of one Fe cation surrounding the O vacancy in the FFF-, FFN-, or FNN-vacancy type structures, as shown in Fig. 9. The calculated magnetic moment, the valence state of the first-row transition metal dopant, and the doping energy released upon substitution of the structural Fe ion are listed in Table VII. Our simulations indicate that the magnetic moment decreases to ~3.70 μ_B in only two Fe cations in the three types of structures as a result of the formation of the oxygen vacancy. We observe that two first NN Fe ions of the oxygen vacancy have a smaller magnetic moment in the FFF- and FFN-type structures,

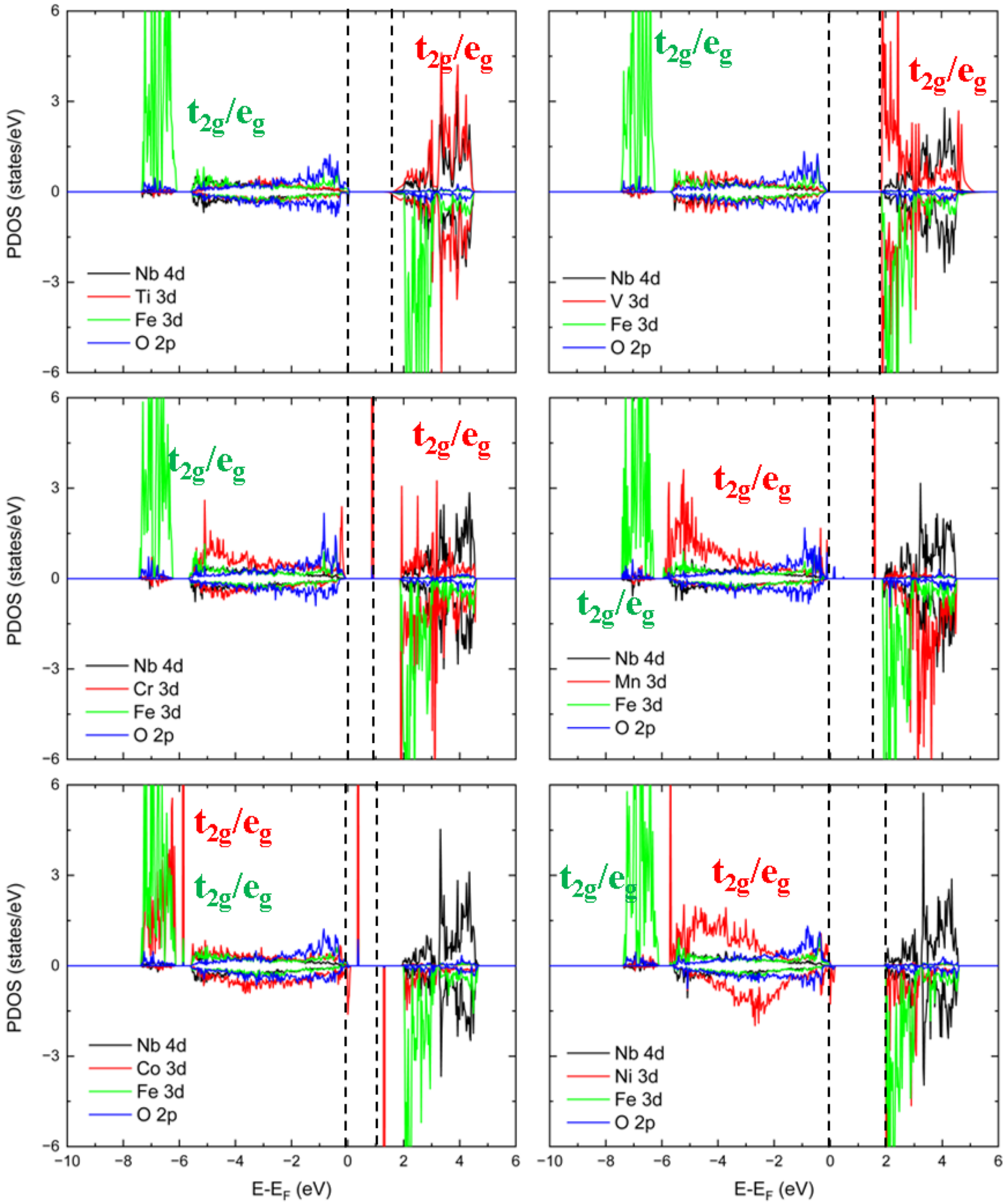

FIG. 7. Projected density of states (PDOS) of $FeNbO_4$ doped with (a) Ti, (b) V, (c) Cr, (d) Mn, (e) Co, and (f) Ni, on the Nb site.

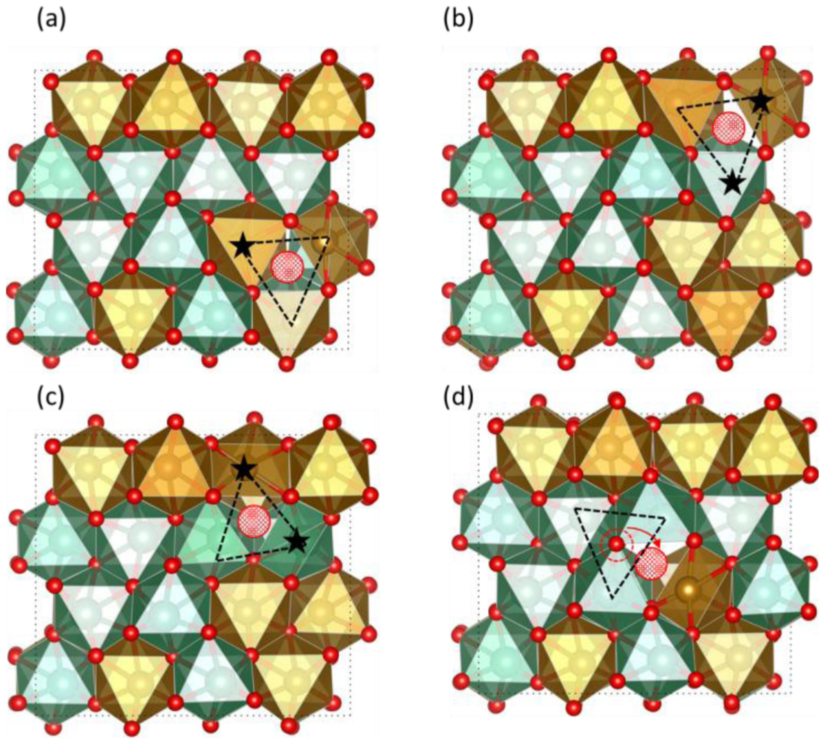

FIG. 8. Optimized structures of four distinct oxygen vacancy types in the $FeNbO_4$ structure: (a) FFF, (b) FFN, (c) FNN, and (d) NNN. The star denotes the selected doping sites. O is red, Fe is brown, and Nb is green.

TABLE VI. Lattice parameters (*a*, *b*, and *c*), lattice angles (α, β, and γ), volume (*V*), and formation energy of oxygen vacancy (E_{vac}) for the O-deficient $FeNbO_4$ structure.

	a (Å)	b (Å)	c (Å)	α (°)	β (°)	γ (°)	V (Å^3)	$\Delta V/V$ (%)	E_{vac} (eV)
Stoichiometric	9.393	11.367	10.127	90.03	89.93	89.68	1081.339	⋯	⋯
FFF	9.409	11.386	10.144	89.94	90.15	89.82	1086.819	0.51	2.14
FFN	9.405	11.383	10.191	90.15	90.27	89.41	1091.086	0.90	3.28
FNN	9.415	11.405	10.180	89.99	89.83	90.17	1093.294	1.10	4.13

whereas one first NN cation and one second NN cation experience a reduction in the magnetic moment in the FNN-type structure. Although underestimated, the calculated magnetic moment of ~3.7 μ_B corresponds to an electronic distribution of $Fe^{e_g\uparrow\uparrow}_{t_{2g}\uparrow\downarrow\uparrow\uparrow}$ for an octahedral Fe^{2+}, as shown in Fig. S4. We found that Ti has the smallest magnetic moment of ~0.80 μ_B of all the dopants considered in this study, where the magnetic moments increase with the atomic number of the transition metal from Ti to Mn, which has the largest value of ~4.57 μ_B. Our calculations also suggest that the magnetic moment decreases from Mn to Co and from Co to Ni. The electronic distributions of $Ti^{e_g}_{t_{2g}\uparrow}$, $V^{e_g}_{t_{2g}\uparrow\uparrow}$, $Cr^{e_g\uparrow}_{t_{2g}\uparrow\uparrow\uparrow}$, $Mn^{e_g\uparrow\uparrow}_{t_{2g}\uparrow\uparrow\uparrow}$, $Co^{e_g\uparrow\uparrow}_{t_{2g}\uparrow\downarrow\uparrow\downarrow\uparrow}$, and $Ni^{e_g\uparrow\uparrow}_{t_{2g}\uparrow\downarrow\uparrow\downarrow\uparrow\downarrow}$ correspond to the valence states +3, +3, +2, +2, +2, and +2, respectively, see Figs. S5–S7. Replacing Fe by Mn and Ni dopants is an energetically favorable process compared to introducing Ti, V, Cr, and Co dopants, displaying the following decreasing order of doping energies $E_{Ti} > E_V > E_{Cr} > E_{Co} > E_{Mn} > E_{Ni}$. The analysis of the magnetic moments suggests that Fe gains one electron, reducing its valence state from 3+ to 2+, upon the formation of the O vacancy in the stoichiometric material, as shown in Tables IV and VII. The calculated magnetic moments and valence states of the transition metal dopant atoms are essentially the same in the three types of O-deficient structures. Moreover, we found that the magnetic moments and electronic structures of the dopant atoms are very similar in both $Fe_{0.9375}A_{0.0625}NbO_4$ and $Fe_{0.9375}A_{0.0625}NbO_{3.9375}$, with the exception of the Cr and Mn dopants. The calculated magnetic moment increases from 2.91 to ~3.6 μ_B and from 3.85 to ~4.5 μ_B for Cr and Mn, respectively, suggesting that the formation of the O vacancy reduces these cations from the 3+ to the 2+ oxidation state. Only Cr and Mn display a larger magnetic moment, corresponding to a reduction from 3+ to 2+ with respect to the

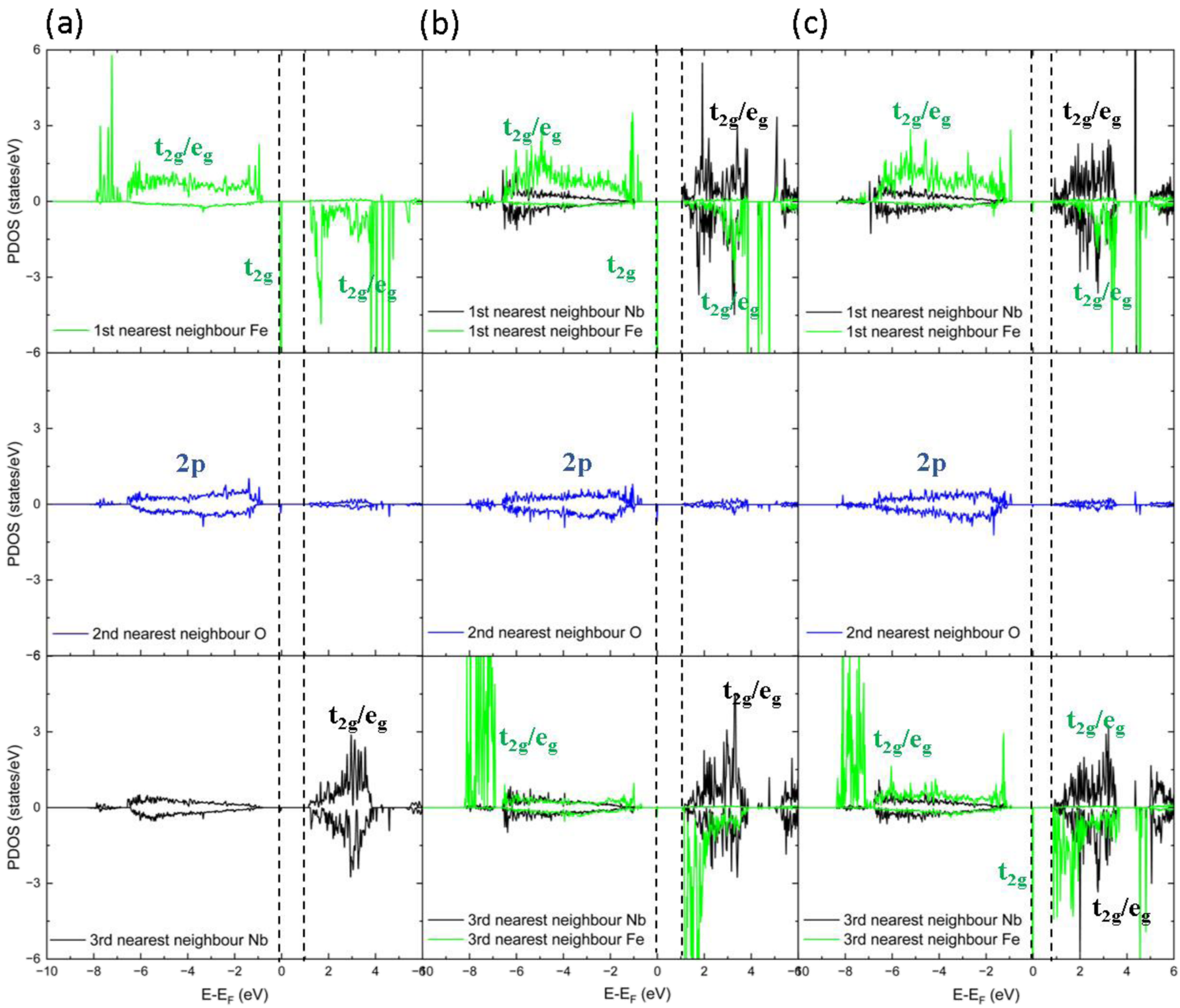

FIG. 9. Projected density of states (PDOS) for $FeNbO_4$ with different types of oxygen vacancies: (a) FFF, (b) FFN, and (c) FNN.

doped material without O vacancies, in agreement with the charge of Fe^{2+} that they substituted. However, Ti and V, which have a valence state of 3+ donated one electron to the first or third NN Fe cations. The doping energy for Ti, V, Cr, and Mn (Co and Ni) decreases (increases) from the FFF- to the FFN-type and from the FFN- to the FNN-type O-deficient structure. Our calculated doping energies suggest that replacing Fe with Ti^{3+} and V^{3+} is thermodynamically less favorable than doping with the other cations in the 3+ oxidation state. We found that the total energy differences ($E_t = E_{vac} + E_{doping}$) between the stoichiometric and doped O-deficient materials are still larger for the FNN-type structure, with the exception of the Ti-doped phase, indicating that doping and partial reduction cannot enhance its stability with respect to the FFF- and FFN-type structures.

Next, we introduced dopants on the fivefold Nb sites in proximity to the oxygen vacancies and subsequently relaxed the structures before computing their properties, as detailed in Table VIII. The FFF-type vacancy structure was not considered for Nb site doping due to the absence of a first NN Nb site. Our simulations indicate that magnetic moments remain zero for all Nb atoms within the FFN- and FNN-type vacancy structures. The magnetic moment of the dopants progressively increases with atomic number from Ti to Mn, while it decreases from Mn to Ni. The magnetic moment configurations for the first-row transition metal atoms correspond to $Ti^{e_g}_{t_{2g}}$, $V^{e_g}_{t_{2g}\uparrow}$, $Cr^{e_g}_{t_{2g}\uparrow\uparrow\uparrow}$, $Mn^{e_g\uparrow}_{t_{2g}\uparrow\uparrow\uparrow}$, $Co^{e_g\uparrow\uparrow}_{t_{2g}\uparrow\downarrow\uparrow\downarrow\uparrow\downarrow}$, and $Ni^{e_g\uparrow\downarrow\uparrow}_{t_{2g}\uparrow\downarrow\uparrow\downarrow\uparrow\downarrow}$. We have inferred valence states of +4 for Ti, +4 for V, +3 for Cr, +3 for Mn, +1 for Co, and +1 for Ni. Our calculated doping energies reveal that

TABLE VII. Atomic magnetic moments (m_s), valence states (VS), doping energy (E_d), and energy differences (E_t) of the O-deficient $FeNbO_4$ structure with dopants in the Fe site.

	FFF (Fe site)				FFN (Fe site)				FNN (Fe site)			
A	m_s (μ_B)	VS	E_d (eV)	E_t (eV)	m_s (μ_B)	VS	E_d (eV)	E_t (eV)	m_s (μ_B)	VS	E_d (eV)	E_t (eV)
Fe first neigh	3.73 (2)	+2	⋯	⋯	3.72(2)	+2	⋯	⋯	3.7 (1)	+2	⋯	⋯
Fe third neigh	⋯	⋯	⋯	⋯	⋯	⋯	⋯	⋯	3.73(1)	+2		⋯
Ti	0.84	+3	3.72	5.86	0.82	+3	3.31	6.59	0.80	+3	2.01	6.14
V	1.89	+3	1.53	3.67	1.86	+3	1.39	4.67	1.84	+3	1.28	5.41
Cr	3.60	+2	0.91	3.05	3.60	+2	0.76	4.04	3.57	+2	0.68	4.81
Mn	4.57	+2	−0.28	1.86	4.56	+2	−0.32	2.96	4.55	+2	−0.34	3.79
Co	2.75	+2	0.27	2.41	2.71	+2	0.35	3.63	2.74	+2	0.36	4.49
Ni	1.74	+2	−0.79	1.35	1.70	+2	−0.68	2.60	1.73	+2	−0.55	3.58

TABLE VIII. Atomic magnetic moments (m_s), valence states (VS), doping energy (E_d), and energy differences (E_t) of the O-deficient $FeNbO_4$ structure with dopants incorporated into the Nb site.

	FFN (Nb site)				FNN (Nb site)			
A, B	m_s (μ_B)	VS	E_d (eV)	E_t (eV)	m_s (μ_B)	VS	E_d (eV)	E_t (eV)
Nb	0	+5	⋯	⋯	0	+5	⋯	⋯
Ti	0	+4	0.27	3.55	0	+4	0.38	4.51
V	1.00	+4	0.4	3.68	1.00	+4	0.79	4.92
Cr	2.92	+3	5.47	8.75	2.91	+3	4.76	8.89
Mn	3.89	+3	−0.78	2.50	3.84	+3	−0.65	3.48
Co	2.04	+1	5.91	9.19	2.09	+1	5.32	9.45
Ni	1.47	+1	−0.26	3.02	1.45	+1	−0.24	3.89

the insertion of Ti, V, and especially Cr and Co into the Nb sites is thermodynamically more difficult than the incorporation of Mn and Ni, with exothermic doping energies of approximately −0.7 and −0.25 eV, respectively. Generally, the generation of oxygen vacancies does not alter the magnetic moment, electronic structure, or oxidation state of Nb^{5+} in $FeNbO_{3.9375}$ compared to $FeNbO_4$. Specifically, the formation of the oxygen vacancy in the doped material leads to changes in the magnetic moments of V, Cr, Mn, and Co from 0 to 1 μ_B, 1.60 to ~2.90 μ_B, 3.03 to ~3.80 μ_B, and 2.59 to ~2.0 μ_B, respectively, corresponding to a reduction in their oxidation states from +5 to +4, +4 to +3, +4 to +3, and +2 to +1. Furthermore, we observed that the oxidation state of each dopant is smaller than that of the removed Nb^{5+} ion. For instance, the 1+ cations received one electron from each Fe^{2+} and one electron from two second NN O atoms, whereas the 3+ and 1+ cations received charge density from one or two Fe^{2+} ions, respectively. We found that Mn and Ni are the only dopants that can be inserted spontaneously into both the Fe and Nb sites, with Mn displaying a larger preference for the Nb position and Ni for the Fe site. Ti and V are thermodynamically more favorable to dope into the Nb than the Fe site for each vacancy-type structure, whereas Cr and Co preferentially substitute Fe rather than Nb. The largest total energy difference for $FeNb_{0.9375}B_{0.0625}O_{3.9375}$ was calculated for the FNN-type structure, suggesting that doping is unable to modify the order of stability of the doped O-deficient materials.

2. Projected density of states (PDOS)

Here, we discuss the PDOS of ions proximate to the oxygen vacancy in the undoped and doped structures. In the FFF-vacancy type configuration, we selected the three Fe ions, positioned as the first NN to the O vacancy at ~2.0 Å, and the five Nb atoms, situated as the third NN within the range of 3.2–4.0 Å, see Fig. S10. In the FFN-vacancy type arrangement, we focused on the two Fe and the sole Nb cations, serving as the first NN of the O vacancy at around 2.0 Å. For the FNN-vacancy type structure, we considered the lone Fe and the two Nb ions, constituting the first NN of the O vacancy at ~2 Å. The PDOS was plotted utilizing the twelve O anions from the three vacancy-type structures (second NN of the O vacancy between 2.6 and 3.4 Å) as well as the three Fe and two Nb ions from the FFN- and FNN-vacancy type structures (third NN of the O vacancy between 3.4 and 4.4 Å), to plot the PDOS, shown in Figs. S11–S13.

Figure 9 illustrates that the t_{2g} and e_g levels in the majority spin channel between −8.0 and −1.5 eV are fully occupied for the first NN Fe ions of the O vacancy in the FFF-vacancy type structure. In the FFN-vacancy type structure, the t_{2g} and e_g orbitals of the first NN Fe are distributed in the majority spin region from −7 to −1 eV. Our calculations suggest that the minority spin channel remains empty in $FeNbO_4$ for the first NN Fe ions in both the FFF- and FFN-vacancy type structures, with the exception of part of the highly localized t_{2g} orbital just below the Fermi level. The t_{2g} and e_g states of the first NN Fe are located in the majority spin channel, while the orbitals in the minority spin channel are unoccupied in the FNN-vacancy type structure. The majority and minority spin channels of the 3d orbitals of the first NN Nb of the O vacancy are symmetric, and their density of states is smaller for the valence than for the conduction band in both the FFN- and FNN-type vacancy structures. We found that the full 2p orbitals of all the second NN oxygen remain delocalized from −7 to −1 eV with respect to the stoichiometric material. For the third NN Nb in the FFF-type vacancy configuration, the negligibly occupied 3d states appear from −7 to −1 eV, whereas the localized states are above 1.0 eV, similar to the FFN- and FNN-type structures. Our simulations indicate that the t_{2g} and e_g levels

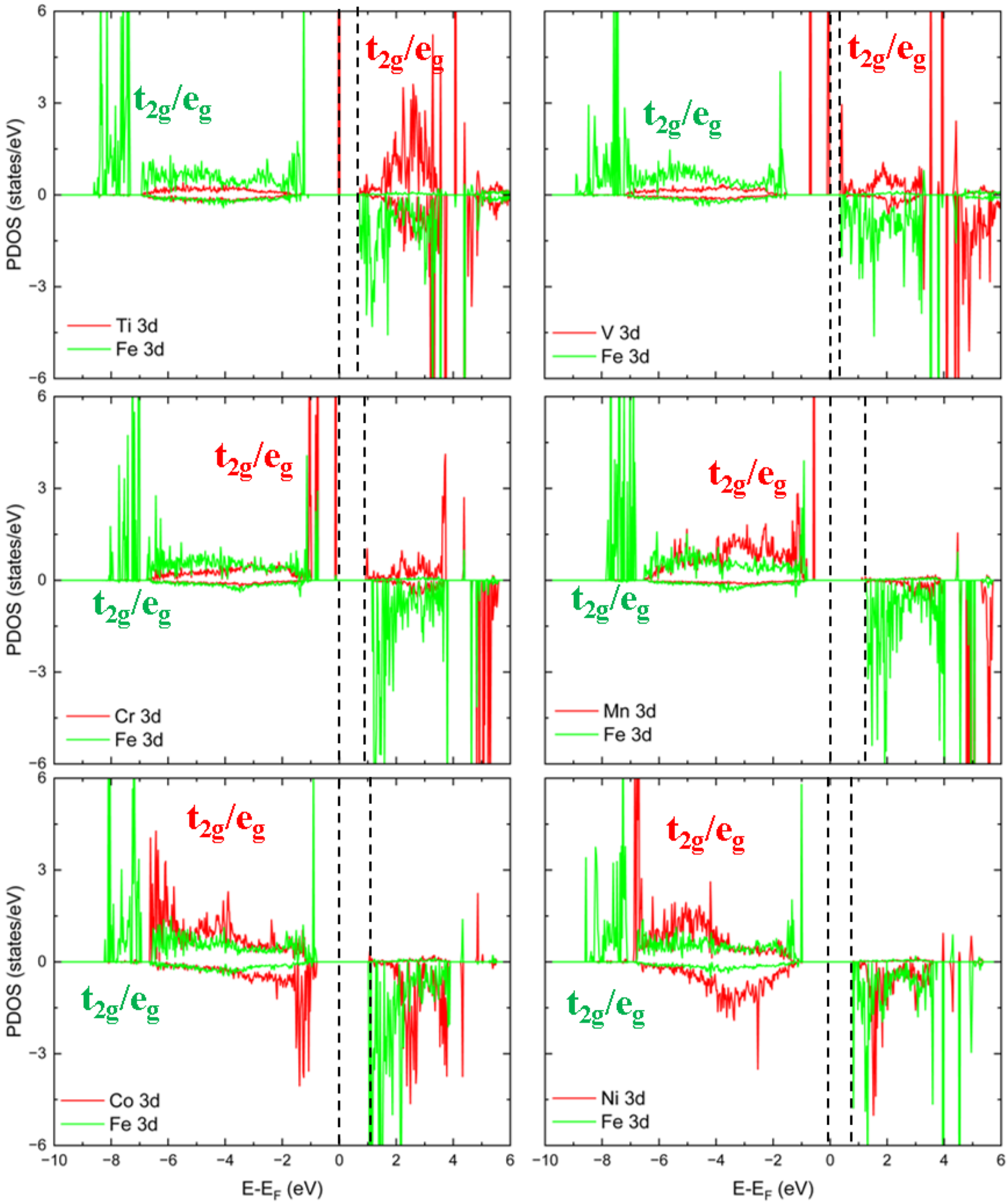

FIG. 10. Projected density of states (PDOS) for dopants and the first nearest neighbor (NN) Fe in the FFF-type $Fe_{0.9375}A_{0.0625}NbO_{3.9375}$ structures with (a) Ti, (b) V, (c) Cr, (d) Mn, (e) Co, and (f) Ni dopants on the Fe site.

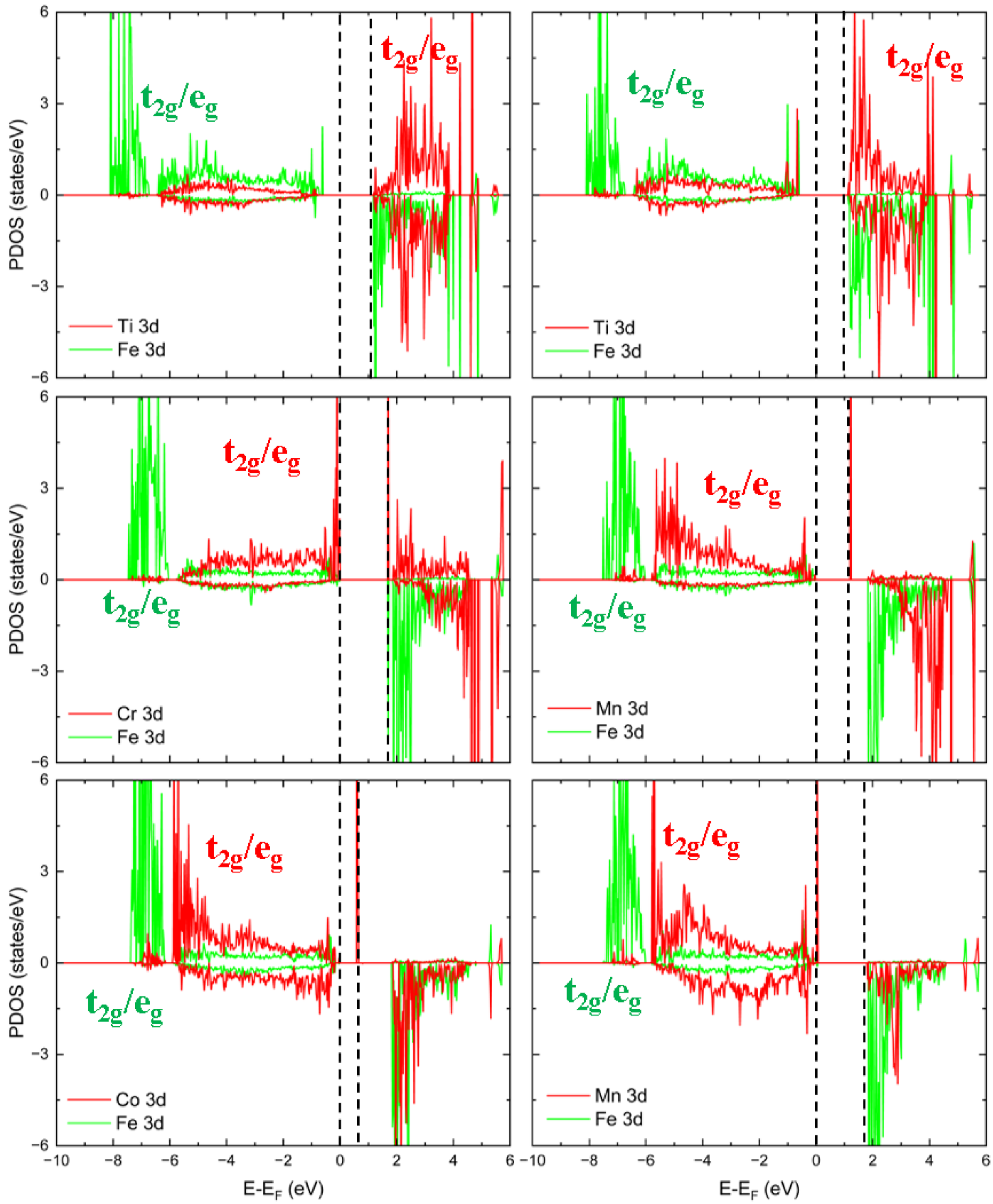

FIG. 11. Projected density of states (PDOS) of the dopants, the first and third nearest neighbor (NN) Fe in the FFN-type $Fe_{0.9375}A_{0.0625}NbO_{3.9375}$ structures with (a) Ti, (b) V, (c) Cr, (d) Mn, (e) Co, and (f) Ni dopants on the Nb site.

of the third NN Fe cations are occupied in the majority spin channel in the FFN- and FNN-type vacancy structures. Interestingly, we found that part of the occupied t_{2g} state of the third NN Fe appears highly localized below the Fermi level in the FNN-vacancy type structure.

Our calculations show that the first NN Fe cations of the O vacancy act as donor levels in the FFF- and FFN-type vacancy structures, reducing the bandgap by ~1.2 eV compared to the stoichiometric configuration. This behavior has also been observed in other O-deficient materials such as $LaFe_{1-x}Nb_xO_3$ and Li_2FeSiO_4.[51,52] However, the electron in this highly localized orbital is derived from the third NN Fe in the FNN-vacancy type structure, suggesting a preference for electron conduction in the rather more remote area from the FNN-type vacancy. The absence of localized Fe t_{2g} and e_g states around −8 eV implies the absence of Fe^{3+} in the vicinity of the vacancy sites, specifically in the first NN region of the FFN- and FNN-type structures. Our calculations indicate that the 3d electronic states of Nb, regardless of their positions, slightly hybridize with the 2p orbitals of oxygen in the valence band, similar to the stoichiometric $FeNbO_4$. Consequently, we opted not to discuss their density of states in the subsequent sections.

First, we have simulated the PDOS for $Fe_{0.9375}A_{0.0625}NbO_{3.9375}$ structures, containing FFF-, FFN-, and FNN-type vacancies, respectively, see Figs. S13–S15. Overall, we found that the electronic states of the dopants and Fe cations exhibited similar distributions in the three types of oxygen-vacancy structures. In this context, we chose to analyze only the PDOS of the doped FFF-vacancy type configuration to investigate the effect of dopants on the electronic structures.

Figure 10 illustrates that the 3d orbitals of the first NN Fe occupy the majority spin channel from −8 to −1 eV, while the minority spin channel remains unfilled above 1 eV in all the doped structures. The electronic states of Ti, V, and Co dopants are primarily distributed in the conduction region, with one, two, and four sharp orbitals, respectively, appearing below the Fermi level. The majority spin channel of the Mn dopant is fully occupied, while its minority spin channel is in the conduction region. The t_{2g} and e_g levels of the Co and Ni dopants are present in both the majority and minority spin channels in the valence region, and part of the conduction band remains unoccupied over 1 eV. In general, our simulations reveal that the highly localized states of Fe^{2+} below 0 eV are replaced by the t_{2g} orbitals of the Ti, V, and Cr dopants, reducing the bandgap to less than 0.5 eV, especially for the Ti- and V-doped structures. In contrast, the t_{2g} and e_g levels of the Mn, Co, and Ni dopants shift toward the deep region of the valence band, resulting in no states around the Fermi levels, consistent with observations in doped TiO_2 as well.[38–40] Overall, comparing with the doped $Fe_{0.9375}A_{0.0625}NbO_4$ structures, we observe that the electronic states of Ti and V remain similarly allocated in both doped configurations. Meanwhile, the highly localized orbitals of Cr and Mn are generated below the Fermi levels in the O-deficient structures. The electronic states of the Co and Ni dopants tend to be delocalized in the valence region from −7 to −1 eV in the $Fe_{0.9375}A_{0.0625}NbO_{3.9375}$ structures, rather than being concentrated around −8 eV in the $Fe_{0.9375}A_{0.0625}NbO_4$ configurations.

We also selected the PDOS of the FFN-type $FeNb_{0.9375}B_{0.0625}O_{3.9375}$ materials to illustrate their electronic structures, see Fig. 11, as they exhibit similar distributions to the FNN-type, see Figs. S16 and S17. We observe that the occupied states of the Fe cations are distributed from −8 to −1 eV for the Ti- and V-doped structures and from −8 to 0 eV for the Cr-, Mn-, Co-, and Ni-doped structures. The t_{2g} and e_g levels of the Ti and V dopants predominantly occupy both the majority and minority spin channels in the conduction region, except for the localized t_{2g} orbitals of V near the VBM. Specifically, a sharp level is observed in the CBM of the Cr-doped structure, and this type of highly localized orbitals shifts toward the Fermi levels with an increase in atomic numbers from Cr to Ni. In general, our calculations demonstrate the removal of highly localized orbitals of the Fe cations below the Fermi levels in the Ti- and V-doped structures. Moreover, we found no evidence of Fe^{2+} in the Cr-, Mn-, Co-, and Ni-containing structures, indicating that it has been oxidized back to Fe^{3+} after doping. Furthermore, acceptor levels are generated and tend to move close to the Fermi levels in the Cr- to the Ni-doped structures. During this process, we observe a reduction in the bandgap to 0.5 eV for the Co-doped structure, while it remains relatively large at −1.8 eV for the Cr- and Ni-doped structures, even exceeding that of the undoped O-deficient structures. When comparing with the $FeNb_{0.9375}B_{0.0625}O_4$ structure, we found that the electronic state distributions of Ti dopants remain the same, whereas the additional localized levels of V dopants are situated in the VBM after the generation of oxygen vacancies. The acceptor level, composed of the 3d orbitals of Cr, tends to move toward the CBM after the creation of oxygen vacancies. For the Mn-, Co-, and Ni-doped configurations, the impact of the oxygen vacancy on the electronic structures of the dopant is negligible and can be disregarded.

IV. CONCLUSIONS

We have conducted DFT calculations of the $Fe_{0.9375}A_{0.0625}NbO_4$ and $FeNb_{0.9375}B_{0.0625}O_4$ materials, where A, B = Ti, V, Cr, Mn, Co, and Ni, as well as the O-deficient $Fe_{0.9375}A_{0.0625}NbO_{3.9375}$ and $FeNb_{0.9375}B_{0.0625}O_{3.9375}$ structures. Our calculations indicate that substituting the Fe cation with these dopants is considerably more energetically favorable than the Nb site, leading to significant compression of $FeNb_{0.9375}B_{0.0625}O_4$, except for the Ti-doped configuration. Doping Ti, V, and Mn at the Fe site of the stoichiometric structure transforms it into an n-type semiconductor, while the Co- and Ni-doped $FeNb_{0.9375}B_{0.0625}O_4$ structures shift to p-type semiconductors.

In the O-deficient structure, a random distribution of cations occurs, resulting in the identification of three stable types of oxygen vacancies, i.e., FFF-, FFN-, and FNN-type vacancies. Our calculations have shown that the stability of O-deficient configurations depends on the number of first NN Nb atoms at the O vacancy. For instance, generating the FFF-type vacancy is less endothermic than the FNN-type vacancy, leading to the largest volume expansion. Overall, for the doping process in the Fe or Nb sites surrounding the vacancies, we observe that the type of oxygen vacancies does not significantly affect the structural properties and electronic structures of the dopants. However, the presence of an oxygen vacancy can alter the oxidation state and doping energies relative to the $Fe_{0.9375}A_{0.0625}NbO_4$/$FeNb_{0.9375}B_{0.0625}O_4$ structures. For instance, the order of doping energies in the Fe sites of the non-vacancy configurations is as follows: $E_{Ti^{3+}} > E_{Co^{2+}} > E_{Ni^{2+}} > E_{V^{3+}} > E_{Mn^{3+}} > E_{Cr^{3+}}$, whereas in the O-deficient structures, the sequence becomes $E_{Ti^{3+}} > E_{V^{3+}} > E_{Cr^{2+}} > E_{Co^{2+}} > E_{Mn^{2+}} > E_{Ni^{2+}}$. Furthermore, it is noteworthy that doping Ti and V into the Fe sites of the O-deficient structures could significantly enhance electronic conduction by moving the donor levels close to the CBM. However, doping these first-row transition metals into the Nb site surrounding the vacancies tends to shift the structures toward p-type semiconductors, especially for the Co-doped configurations, where the bandgap narrows from 1.0 to 0.5 eV.

SUPPLEMENTARY MATERIAL

The supplementary material includes the structural information of metal oxides used for calculating doping energies; the relationship between volume change, bandgap, and d-band center; the magnetic configurations; the octahedral field of splitting; the selected sites for doping atoms; and the PDOS plots of the O-deficient structures.

ACKNOWLEDGMENTS

Xingyu Wang acknowledges the China Scholarship Council (CSC) (Grant No. 201906460008) and the University of Leeds for the award of a Ph.D. scholarship. This work has used the computing resources from the Supercomputing Wales project, which is partly funded by the European Regional Development Fund (ERDF), and the high-performance computing facilities (ARC4) provided by the University of Leeds. We also acknowledge computing resources on the UK's national supercomputing service ARCHER2 facility (http://www.archer2.ac.uk) via our membership of the UK's HEC Materials Chemistry Consortium, which is funded by EPSRC (Grant No. EP/X035859). For the purpose of Open Access, the author has applied a CC BY public copyright licence to any Author Accepted Manuscript version arising from this submission.

AUTHOR DECLARATIONS

Conflict of Interest

The authors have no conflicts to disclose.

Author Contributions

Xingyu Wang: Conceptualization (equal); Formal analysis (equal); Investigation (equal); Methodology (equal); Visualization (equal); Writing – original draft (equal). **David Santos-Carballal**: Conceptualization (equal); Formal analysis (equal); Methodology (equal); Supervision (equal); Writing – original draft (equal); Writing – review & editing (equal). **Nora H. de Leeuw**: Conceptualization (equal); Funding acquisition (equal); Project administration (equal); Resources (equal); Supervision (equal); Writing – review & editing (equal).

DATA AVAILABILITY

All data that support the findings of this study are available within the article and the supplementary material.

REFERENCES

[1] S. Ananta, R. Brydson, and N. W. Thomas, "Synthesis, formation and characterisation of $FeNbO_4$ powders," J. Eur. Ceram. Soc. **19**, 489–496 (1999).
[2] R. Theissmann, H. Ehrenberg, H. Weitzel, and H. Fuess, "Domain structure and lattice strains in $FeNbO_4$," Solid State Sci. **7**, 791–795 (2005).
[3] R. Theissmann, H. Ehrenberg, H. Weitzel, and H. Fuess, "Nanostructured cation distribution in $FeNbO_4$: A synchrotron powder diffraction and transmission electron microscopy investigation," J. Mater. Sci. **37**, 4431–4436 (2002).
[4] D. Saritha, "Sol-gel synthesis and electrochemical properties of wolframite $FeNbO_4$," J. Phys.: Conf. Ser. **1495**, 012019 (2020).
[5] C. Balamurugan, A. R. Maheswari, D. W. Lee, and A. Subramania, "Selective ethanol gas sensing behavior of mesoporous n-type semiconducting $FeNbO_4$ nanopowder obtained by niobium–citrate process," Curr. Appl. Phys. **14**, 439–446 (2014).
[6] S. Kanti Biswas, T. Gnanasekaran, T. Kumar Ghorai, and P. Pramanik, "Sensing properties of chemically synthesized pristine and Pt-impregnated nanosized $FeNbO_4$ in hydrogen, ammonia, and LPG," J. Electrochem. Soc. **155**, J26–J31 (2008).
[7] K. I. Gnanasekar, V. Jayaraman, E. Prabhu, T. Gnanasekaran, and G. Periaswami, "Electrical and sensor properties of $FeNbO_4$: A new sensor material," Sens. Actuators, B **55**, 170–174 (1999).
[8] W. Harrison and A. K. Cheetham, "Structural and magnetic properties of $FeNbO_4$-II," Mater. Res. Bull. **24**, 523–527 (1989), Chemical Crystallography Laboratory, University of Oxford.
[9] G. Alvarez, R. Font, J. Portelles, O. Raymond, and R. Zamorano, "Paramagnetic resonance and non-resonant microwave absorption in iron niobate," Solid State Sci. **11**, 881–884 (2009).
[10] O. Raymond, R. Font, N. Suárez-Almodovar, J. Portelles, and J. M. Siqueiros, "Frequency-temperature response of ferroelectromagnetic $Pb(Fe_{1/2}Nb_{1/2})O_3$ ceramics obtained by different precursors. Part I. Structural and thermo-electrical characterization," J. Appl. Phys. **97**, 084108 (2005).
[11] Q. J. Li *et al.*, "The colossal dielectric properties of $FeNbO_4$," J. Alloys Compd. **616**, 577–580 (2014).
[12] S. Devesa, M. P. Graça, F. Henry, and L. C. Costa, "Dielectric properties of $FeNbO_4$ ceramics prepared by the sol-gel method," Solid State Sci. **61**, 44–50 (2016).
[13] S. Devesa, M. P. Graça, and L. C. Costa, "Microwave dielectric properties of the binary system $BiNbO_4$–$FeNbO_4$," ECS J. Solid State Sci. Technol. **9**, 093010 (2020).
[14] T. Sri Devi Kumari, R. Vinith Gandhi, G. Rahul, G. Kamalanathan, T. Prem Kumar, D. Jeyakumar, and N. Lakshminarasimhan, "Electrochemical lithium insertion behavior of $FeNbO_4$: Structural relations and *in situ* conversion into $FeNb_2O_6$ during carbon coating," Mater. Chem. Phys. **145**, 425–433 (2014).
[15] T. Wang, S. Shi, F. Kong, G. Yang, B. Qian, and F. Yin, "The role of stable interface in nano-sized $FeNbO_4$ as anode electrode for lithium-ion batteries," Electrochim. Acta **203**, 206–212 (2016).
[16] T. Wang, T. Ge, S. Shi, M. Wu, and G. Yang, "Synthesis of wolframite $FeNbO_4$ nanorods as a novel anode material for improved lithium storage capability," J. Alloys Compd. **740**, 7–15 (2018).
[17] C. Ni, J. Feng, J. Cui, J. Zhou, and J. Ni, "An *n*-type oxide $Fe_{0.5}Mg_{0.25}Ti_{0.25}Nb_{0.9}MO_{0.1}O_{4-\Delta}$ for both cathode and anode of a solid oxide fuel cell," J. Electrochem. Soc. **164**, F283–F288 (2017).
[18] H. Zhang, Y. K. Kim, H. Y. Jeong, and J. S. Lee, "A few atomic $FeNbO_4$ overlayers on hematite nanorods: Microwave-induced high temperature phase for efficient photoelectrochemical water splitting," ACS Catal. **9**, 1289–1297 (2018).
[19] X. Liu, D. Xie, J. T. S. Irvine, J. Ni, and C. Ni, "An $FeNbO_4$-based oxide anode for a solid oxide fuel cell (SOFC)," Electrochim. Acta **335**, 135692 (2020).
[20] X. Liu, J. Zhou, D. Xie, J. Ni, and C. Ni, "$FeNbO_4$-Based oxide cathode for steam electrolysis," Solid State Ionics **345**, 115181 (2020).

[21] S. H. Ahmed, M. Bakiro, and A. Alzamly, "Visible-light-driven photocatalytic formation of propylene carbonate using $FeNbO_4$/reduced graphene oxide composites," Materialia **12**, 100781 (2020).
[22] H. Leiva, K. Sieber, B. Khazai, K. Dwight, and A. Wold, "Structural and electronic relationships between conducting iron niobates and iron tungstates," J. Solid State Chem. **44**, 113–118 (1982).
[23] E. Schmidbauer and J. Schneider, "Electrical resistivity, thermopower, and Fe Mossbauer study of $FeNbO_4$," J. Solid State Chem. **134**, 253–264 (1997).
[24] S. He, H. Dai, G. Cai, H. Chen, and L. Guo, "Optimization of $La_{0.75}Sr_{0.25}Cr_{0.5}Mn_{0.5}O_{3-\Delta}$–$Ce_{0.8}Sm_{0.2}O_{1.9}$ compositionally graded anode functional layer," Electrochim. Acta **152**, 155–160 (2015).
[25] X.-F. Ye, S. R. Wang, Z. R. Wang, Q. Hu, X. F. Sun, T. L. Wen, and Z. Y. Wen, "Use of $La_{0.75}Sr_{0.25}Cr_{0.5}Mn_{0.5}O_3$ materials in composite anodes for direct ethanol solid oxide fuel cells," J. Power Sources **183**, 512–517 (2008).
[26] S. Zhang, Y. Wan, Z. Xu, S. Xue, L. Zhang, B. Zhang, and C. Xia, "Bismuth doped $La_{0.75}Sr_{0.25}Cr_{0.5}Mn_{0.5}O_{3-\Delta}$ perovskite as a novel redox-stable efficient anode for solid oxide fuel cells," J. Mater. Chem. A **8**, 11553–11563 (2020).
[27] L. Gan, L. Ye, C. Ruan, S. Chen, and K. Xie, "Redox-reversible iron orthovanadate cathode for solid oxide steam electrolyzer," Adv. Sci. **3**, 1500186 (2016).
[28] K. Kousi, C. Tang, I. S. Metcalfe, and D. Neagu, "Emergence and future of exsolved materials," Small **17**, e2006479 (2021).
[29] P. I. Cowin, R. Lan, L. Zhang, C. T. G. Petit, A. Kraft, and S. Tao, "Study on conductivity and redox stability of iron orthovanadate," Mater. Chem. Phys. **126**, 614–618 (2011).
[30] X. Wang, D. Santos-Carballal, and N. H. de Leeuw, "Oxygen diffusion in the orthorhombic $FeNbO_4$ material: A computational study," Phys. Chem. Chem. Phys. **25**, 6797–6807 (2023).
[31] X. Wang, D. Santos-Carballal, and N. H. de Leeuw, "Density functional theory study of monoclinic $FeNbO_4$: Bulk properties and water dissociation at the (010), (011), (110), and (111) surfaces," J. Phys. Chem. C **125**, 27566–27577 (2021).
[32] S. H. Ahmed, M. Bakiro, and A. Alzamly, "Effect of pH and surfactant on band gap properties of monoclinic $FeNbO_4$ prepared via different routes," Nano-Struct. Nano-Objects **20**, 100400 (2019).
[33] J. Koenitzer, B. Khazai, J. Hormadaly, R. Kershaw, K. Dwight, and A. Wold, "Preparation and photoelectronic properties of $FeNbO_4$," J. Solid State Chem. **35**, 128–132 (1980).
[34] G. Kresse and J. Furthmiiller, "Efficiency of *ab-initio* total energy calculations for metals and semiconductors using a plane-wave basis set," Comput. Mater. Sci. **6**, 15–20 (1996).
[35] G. Kresse and J. Furthmuller, "Efficient iterative schemes for *ab initio* total-energy calculations using a plane-wave basis set," Phys. Rev. B **54**, 11169–11186 (1996).
[36] G. Kresse and J. Hafner, "*Ab initio* molecular dynamics for open-shell transition metals," Phys. Rev. B **48**, 13115–13118 (1993).
[37] G. Kresse and J. Hafner, "Norm-conserving and ultrasoft pseudopotentials for first-row and transition elements," J. Phys.: Condens. Matter **6**, 8245–8257 (1994).
[38] P. E. Blochl, "Projector augmented-wave method," Phys. Rev. B **50**, 17953–17979 (1994).
[39] A. Vega, J. Dorantes-Davila, L. C. Balbas, and G. M. Pastor, "Calculated *sp*-electron and *spd*-hybridization effects on the magnetic properties of small Fe_N clusters," Phys. Rev. B **47**, 4742–4746 (1993).
[40] O. Diéguez, M. M. G. Alemany, C. Rey, P. Ordejón, and L. J. Gallego, "Density-functional calculations of the structures, binding energies, and magnetic moments of Fe clusters with 2 to 17 atoms," Phys. Rev. B **63**, 205407 (2001).
[41] J. P. Perdew, K. Burke, and M. Ernzerhof, "Generalized gradient approximation made simple," Phys. Rev. Lett. **77**, 3865–3868 (1996).
[42] S. L. Dudarev, G. A. Botton, S. Y. Savrasov, C. J. Humphreys, and A. P. Sutton, "Electron-energy-loss spectra and the structural stability of nickel oxide: An LSDA+U study," Phys. Rev. B **57**, 1505–1509 (1998).
[43] G. Henkelman, A. Arnaldsson, and H. Jónsson, "A fast and robust algorithm for Bader decomposition of charge density," Comput. Mater. Sci. **36**, 354–360 (2006).
[44] H. D. Luong, H. Momida, V. A. Dinh, and T. Oguchi, "Understanding doping effects on P2 $Na_xMn_{1-y}M_yO_2$ (M = Li, Mg, Al, Ti, V, Cr, Fe, Co, Ni) cathode materials for Na-ion batteries," Phys. Rev. Mater. **6**, 015802 (2022).
[45] R. Prasad, R. Benedek, and M. M. Thackeray, "Dopant-induced stabilization of rhombohedral $LiMnO_2$ against Jahn–Teller distortion," Phys. Rev. B **71**, 134111 (2005).
[46] M. A. Halcrow, "Jahn–Teller distortions in transition metal compounds, and their importance in functional molecular and inorganic materials," Chem. Soc. Rev. **42**, 1784–1795 (2013).
[47] D. Santos-Carballal, A. Roldan, R. Grau-Crespo, and N. H. de Leeuw, "A DFT study of the structures, stabilities and redox behaviour of the major surfaces of magnetite Fe_3O_4," Phys. Chem. Chem. Phys. **16**, 21082–21097 (2014).
[48] D. S. Aidhy, B. Liu, Y. Zhang, and W. J. Weber, "Chemical expansion affected oxygen vacancy stability in different oxide structures from first principles calculations," Comput. Mater. Sci. **99**, 298–305 (2015).
[49] B. Choudhury and A. Choudhury, "Ce^{3+} and oxygen vacancy mediated tuning of structural and optical properties of CeO_2 nanoparticles," Mater. Chem. Phys. **131**, 666–671 (2012).
[50] M. W. J. Chase, *NIST JANAF Termochemical Tables* (American Chemical Society and American Institute of Physics for the National Institute of Standards and Technology, Washington DC, 1998).
[51] Y. Zhou, Z. Lü, J. Li, S. Xu, D. Xu, and B. Wei, "The electronic properties and structural stability of $LaFeO_3$ oxide by niobium doping: A density functional theory study," Int. J. Hydrogen Energy **46**, 9193–9198 (2021).
[52] L. Zhang, S. Wu, J. Shuai, Z. Hou, and Z. Zhu, "Formation of oxygen vacancies in Li_2FeSiO_4: First-principles calculations," Phys. Chem. Chem. Phys. **23**, 20444–20452 (2021).